J. Fluid Mech. (2008), *vol.* 605, *pp.* 367–387. © 2008 Cambridge University Press
doi:10.1017/S0022112008001559 Printed in the United Kingdom

Collisions of solid particles with vortex rings in superfluid helium

DEMOSTHENES KIVOTIDES AND S. LOUISE WILKIN

Center for Risk Studies and Safety, Department of Chemical Engineering, University of California, Santa Barbara, CA 93117, USA

(Received 28 January 2008 and in revised form 15 March 2008)

We have performed self-consistent computations of the interactions between a superfluid vortex-ring and a solid particle for two different vortex-ring sizes and over a wide range of temperatures. In all cases, the particle and the vortex eventually separate. For temperature $T = 0$ K, larger rings tend to trap the particle more effectively than smaller rings. Trying to escape the vortex, the particle follows a spiralling trajectory that could be experimentally detected. The dominant dynamical process is the excitation and propagation of Kelvin waves along the vortices. For $T > 0$ K, particle–vortex collision induces particle vibrations that are normal to the particle's direction of motion and might be experimentally detectable. In contrast to the $T = 0$ K case, smaller rings induce larger particle oscillation velocities. With increasing temperature, enhanced mutual friction damping of Kelvin waves leads to the damping of both the intensity and frequency of post-collision particle vibrations. Moreover, higher temperatures increase the relative impact of the Stokes drag force on particle motion.

1. Introduction

The physics of particle-laden flows can be studied at various space–time scales employing appropriately designed mathematical models (see for example Crowe, Sommerfeld & Tsuji 1998; Drew & Passman 1998; Brennen 2005). One standard method of inquiry assumes that the particles are spherical, and that they are much smaller than the smallest spatial scale of a corresponding pure flow with the same initial and boundary conditions, but without any particles. In turbulent flows, the latter scale could be identified with the Kolmogorov microscale of turbulence. Under these conditions, there is always a creeping flow of very small Reynolds number around the particles, which therefore could justifiably be neglected in comparison to an energetic large-scale flow. A similar accompanying assumption is that the particle field is so dilute, that hydrodynamic interactions between particles could also (most of the time) be neglected. Hence, the solution of the corresponding multi-body Stokes micro-flow problem (with either point or finite-size particles) could be avoided. When such assumptions of one-way coupling are employed, we can use analytical solutions of the flow field around an isolated sphere in a uniform low-Reynolds-number flow stream, in order to find closed-form expressions for the force that the fluid exerts on the particle. Since such expressions take into account analytically the developed microflow around the particle, a direct numerical computation of this flow is not necessary. This method allows an economical and adequate treatment of particle-laden normal-fluid flows, whenever the aforesaid assumptions are valid.

https://doi.org/10.1017/S0022112008001559 Published online by Cambridge University Press

A number of experiments have realized particle-laden flows in liquid helium (Celik & VanSciver 2002; Donnelly *et al.* 2002; Zhang, Celik & VanSciver 2004; Zhang & VanSciver 2005; Bewley, Lathrop & Sreenivasan 2006). The latter are two-component physical systems where a normal fluid interacts via mutual friction forces with a superfluid (Donnelly 1991; Barenghi, Donnelly & Vinen 2001; Vinen & Niemela 2002; Finne *et al.* 2006). At present, there are no methods for the direct unambiguous measurement of the local flow velocity in any of the two fluids. The idea behind these experiments is to release micrometre-sized particles in liquid helium, and by measuring their velocity (via the particle image velocimetry (PIV) technique) to make inferences about the velocity of the two constituent fluids. A first theoretical analysis of such flows was offered by Poole *et al.* (2005). This analysis was based on assumptions very similar to those mentioned above for the treatment of normal multiphase flow. Unfortunately, such an approach encounters severe difficulties when applied to superfluids. In particular, the latter are characterized by quantized potential vortices of nanometre-sized cores which correspond to spatial flow scales that are orders of magnitude smaller than the micrometre-sized diameters of the inserted particles. Because of these, Kivotides, Barenghi & Sergeev (2005, 2006*b*) had to confine themselves to dilute particle fields in order to show that when the particles are located many particle diameters away from superfluid vortices, they are forced by the viscous drag to trace the normal fluid and thus PIV methods could successfully be employed to measure the normal-fluid velocity. Hence, multiphase superfluids require new, more powerful methods for their mathematical description. Kivotides, Barenghi & Sergeev (2006*a*, 2007*b*, 2008) have developed methods for the treatment of particle–vortex interactions from first principles, without any scale separation or one-way coupling hypotheses. In this paper, we first formulate the mathematical problem that corresponds to the collision of a spherical particle with a superfluid vortex ring, and then (using the recently developed methods), we solve this problem for various particle ring configurations of importance to superfluids.

2. Mathematical model

We are concerned with the collision of a superfluid vortex ring of radius R with a solid spherical particle of radius a. In general, let $\boldsymbol{X}(\ell, \mathrm{t})$ denote a superfluid vortex link $\mathscr{L}$ where ℓ is the arclength parameterization along the vortex loopsand t is time. The dynamics of $\boldsymbol{X}(\ell, \mathrm{t})$ are described by the following integrodifferential equation:

$$\frac{\partial \boldsymbol{X}}{\partial t} = \boldsymbol{V}^s + \boldsymbol{V}^b + \boldsymbol{V}^\phi + \boldsymbol{V}^f. \tag{2.1}$$

The first contribution to the right-hand side is the superfluid velocity $\mathbf{V}^s$ that is given by the Biot-Savart integral:

$$\boldsymbol{V}^s(\boldsymbol{x}) = -\frac{\kappa}{4\pi}\int_{\mathscr{L}} \mathrm{d}\ell \frac{\boldsymbol{X}' \times (\boldsymbol{X} - \boldsymbol{x})}{|\boldsymbol{X} - \boldsymbol{x}|^3}, \tag{2.2}$$

where $\boldsymbol{X}' \equiv \partial \boldsymbol{X}/\partial \ell$ is the unit tangent vector (indicating the direction of the singular superfluid vorticity) and κ is the quantum of circulation.

The particle acts like an obstacle that deforms the vortex-induced flow, since the latter cannot penetrate the spherical boundary of the former. This (particle-induced) flow deformation advects the vortices and this effect is denoted by the term $\boldsymbol{V}^b$. The computation of $\boldsymbol{V}^b$ is discussed by Schwarz (1974) and Kivotides *et al.* (2006*a*). The

https://doi.org/10.1017/S0022112008001559 Published online by Cambridge University Press

latter reference provides detailed, instability-free formulae for the computation of $\boldsymbol{V}^b$ that we have employed in this work.

The third contribution $\boldsymbol{V}^\phi$ is the potential flow field induced by the motion of a spherical particle with velocity $\boldsymbol{V}^p$ as it moves ina stationary unbounded inviscid fluid. This flow field is given by the expression (Drew & Passman 1998):

$$\left.\begin{aligned} \boldsymbol{V}^\phi(\boldsymbol{x}|z) &= -0.5\left(\frac{a}{r}\right)^3 \boldsymbol{V}^p(z)\cdot\left(\boldsymbol{I}-3\frac{\boldsymbol{x}'\boldsymbol{x}'}{r^2}\right), \\ V_j^\phi(\boldsymbol{x}|z) &= -0.5\left(\frac{a}{r}\right)^3 V_i^p(z)\left(\delta_{ij}-3\frac{x_i'x_j'}{r^2}\right), \end{aligned}\right\} \tag{2.3}$$

where $\boldsymbol{V}^\phi(\boldsymbol{x}|z)$ is the velocity of the fluid at $\boldsymbol{x}$ caused by a sphere of radius a whose centre is located at z, $\boldsymbol{I}$ is the 3×3 unit matrix whose elements are the Kronecker delta symbols δ_{ij} $(i, j = 1, 2, 3)$, $\boldsymbol{x}' = \boldsymbol{x} - z$, $r = |\boldsymbol{x} - z|$, and a summation over index i is implied in the component form of the equation.

Since in this work we compute evolutions for both pure ($T = 0$ K, where T is the temperature) superfluid helium and superfluid helium at non-zero temperature, we must take into account the effects of the mutual friction force on the vortices. These effects correspond to the fourth term $\mathbf{V}^f$ that is given by the formula:

$$\begin{aligned} \boldsymbol{V}^f = h_{\star\star}(\boldsymbol{V}^s + \boldsymbol{V}^b + \boldsymbol{V}^\phi) + h_\star \boldsymbol{X}'\times(\boldsymbol{V}^n - (\boldsymbol{V}^s + \boldsymbol{V}^b + \boldsymbol{V}^\phi)) \\ + h_{\star\star}\boldsymbol{X}'\times(\boldsymbol{X}'\times\boldsymbol{V}^n), \end{aligned} \tag{2.4}$$

where $\boldsymbol{V}^n$ is the kinematically prescribed normal-fluid velocity, and $h_\star = d_{\star\star}/(d_{\star\star}^2 + (1-d_\star)^2)$, $h_{\star\star} = (d_\star - d_{\star\star}^2 - d_\star^2)/(d_{\star\star}^2 + (1-d_\star)^2)$ are dimensionless numbers given in terms of the (also dimensionless) mutual friction coefficients $d_\star$ and $d_{\star\star}$. To compute the latter coefficients, we start from the Hall–Vinen coefficients and following Barenghi, Donnelly & Vinen (1983) calculate the transverse and longitudinal drag coefficients $D_\star'$ and $D_{\star\star}$. Subsequently, we compute $D_\star = D_\star' - \rho_n\kappa$, and finally $d_\star = D_\star/(\rho_s\kappa)$, $d_{\star\star} = D_{\star\star}/(\rho_s\kappa)$.

The particle dynamics is described by the following equation:

$$m_e\frac{\mathrm{d}\boldsymbol{V}^p}{\mathrm{d}t} = 6\pi a\mu_n(\boldsymbol{V}^n - \boldsymbol{V}^p) + 2\pi\rho_s a^3\frac{\partial \boldsymbol{V}^s(z,t)}{\partial t} + \frac{1}{2}\rho_s\int_S \mathrm{d}S(\boldsymbol{V}^s + \boldsymbol{V}^b)^2\hat{\boldsymbol{n}}, \tag{2.5}$$

where m_e is the effective mass of the particle $m_e = m + (2/3)\pi(\rho_s + \rho_n)a^3$, m is the particle mass, μ_n is the dynamic viscosity of the normal fluid, ρ_s and ρ_n are the superfluid mass density and normal-fluid mass density, respectively, and $\boldsymbol{V}^s(z,t)$ is the vortex-induced velocity at the particle centre. We will consider only neutrally buoyant particles here, thus the particle mass density ρ_p is equal to the sum of the superfluid and normal-fluid mass densities. The last term is a surface integral with $\hat{\boldsymbol{n}}$ being the outward unit radial vector field on the spherical particle surface. It is convenient to write the right-hand side of (2.5) as $\boldsymbol{f} = \boldsymbol{f}_d + \boldsymbol{f}_l + \boldsymbol{f}_b$; this decomposes the total force $\boldsymbol{f}$ into viscous drag, $\boldsymbol{f}_d$, local, $\boldsymbol{f}_l$, and boundary force, $\boldsymbol{f}_b$.

Note that, although the equation of motion for the vortices is exact for both $T = 0$ K and finite-temperature liquid helium, the same is not true for the particle equation of motion. The latter is exact only at $T = 0$ K in which case it reduces to the important Schwarz's solid-particle equation of motion (Schwarz 1974). The equation employed here takes heuristically into account thermal effects via a viscous drag force known as Stokes force (the first term on the right-hand side), and an added mass term on the left-hand side that is non-zero when the particle accelerates inside the normal fluid. An exact treatment of normal-fluid effects could be made

https://doi.org/10.1017/S0022112008001559 Published online by Cambridge University Press

by solving the normal-fluid Navier–Stokes equation around a suspension of solid particles, and taking into account the normal-fluid effect on the particles by replacing the Stokes-drag force in the particle equation of motion by the force

$$f_i^n = \int_S \sigma_{ij} \hat{n}_j \mathrm{d}S, \tag{2.6}$$

where

$$\sigma_{ij} = -p\delta_{ij} + \mu_n\left(\partial V_i^n/\partial x_j + \partial V_j^n/\partial x_i\right) \tag{2.7}$$

is the normal-fluid stress tensor, p is the normal-fluid pressure, repeated indices are summed, and the integral is performed over the particle's surface. This treatment is not within the capabilities of already developed methods and it is a desirable future development.

All computations were performed in an unbounded fluid domain. This was also assumed in Schwarz's derivations of the formulae for $\boldsymbol{V}^b$, as well as of the particle equation of motion at $T = 0$ K. Note, that although the $\boldsymbol{V}^b$ formulae are valid also for vortex loops in periodic domains, the $\boldsymbol{V}^\phi$ formula assumes an isolated particle and does not comply with periodic boundary conditions. The introduction of 'image' particles and their effects on the vortices via the corresponding $\boldsymbol{V}^\phi$ and $\boldsymbol{V}^b$ fields are thus necessary in the latter case. Finally, in all computations of superfluid helium at non-zero temperature reported here, we have prescribed the normal flow kinematically, and we have set $\boldsymbol{V}^n = \boldsymbol{0}$.

3. Mathematical methods

A detailed discussion of the numerical and computational methods is given in Kivotides *et al.* (2008). For completeness of exposition, we provide here a summary. The coupled system of integro-differential equations (2.1) and (2.5) is solved using a third-order-accurate low-storage Runge–Kutta (RK) method. This approach requires the discretization of the Biot-Savart integral in the fashion of Riemann sums. The desingularization of the kernel is achieved by splitting it into local and non-local parts. The local contribution is handled following a method by Schwarz (1985). The non-local contribution is computed by employing a Gaussian kernel in order to smooth the singular superfluid vorticity. The numerical analysis of this method has been described by Winckelmans & Leonard (1993). The method introduces a cutoff scale in the Biot-Savart formula which, in all results reported here, is equal to 1.2 times the discretization length along the vortices. Two vortices reconnect instantaneously when they approach each other at a distance less than the discretization length along their contours. In this way, the small-scale vortex dynamics during reconnection as described by deWaele & Aarts (1994) are not taken into account. This is consistent with the unavailability of very fine spatial resolution along the vortices as dictated by computational complexity constraints. It is also consistent with the aforesaid small distance smoothing of the superfluid singular vorticity according to the Winckelmans–Leonard method.

The method for the computation of $\boldsymbol{V}^b$ was introduced in Schwarz (1985) and the particular computational formulae are available from Kivotides *et al.* (2006*a*). It is based upon an analytical solution in terms of Legendre functions series of the effect of the spherical particle boundary on a linear vortex segment. The treatment of particle–vortex collisions involves a number of important issues that were resolved in Kivotides *et al.* (2008). It builds upon earlier works of Schwarz (1985) and Tsubota &

https://doi.org/10.1017/S0022112008001559 Published online by Cambridge University Press

Maekawa (1993) dealing with vortex collisions with stationary particles, and it extends the latter works in the realm of self-consistent particle–vortex interactions. Kivotides *et al.* (2006*a*) have shown that when a vortex ring propagates in the vicinity of a solid particle, a vortex instability develops and an attachement of the particle to the vortex follows. At first sight, such an attachement leads to discontinuous vortex lines and therefore the Biot-Savart line integral becomes ill-defined. Our method tackles this problem by continuing the attached vortex inside the particle (i.e. by preserving the continuity of the line vortices), and by taking into account in a self-consistent way the effect of the added vortex segments on the dynamics of the vortices outside the particle. These effects include not only Biot-Savart effects of the inner-particle vortex segments on the outer vortices, but also an extra velocity contribution to the outer vortex dynamics which ensures that the addition of inner vortices complies with the no-flow condition normal to the particle's surface. Kivotides *et al.* (2008) provides detailed discussions of the various numerical and computational techniques involved, as well as evidence about the accuracy and efficiency of our approach.

4. Results

We shall apply our methods to ^{4}He. Since superfluidity in ^{4}He exists over a temperature range starting from $T = 0$ K where only the superfluid is present, to a temperature (infinitesimally) below that of the Bose–Einstein condensation where the superfluid component is negligible, a thorough investigation of every superfluid problem ought to include a temperature space parameter search. In this work, we compute particle–vortex-ring interactions at four different temperatures: $T = 0$ K (where $\rho_s = 0.145\,\mathrm{g\ cm^{-3}}$ and $\rho_n = 0$), $T = 1.3$ K (where $\rho_s = 0.1386$ g cm^{-3}, $\rho_n = 0.00652$ g cm^{-3} and $\mu_n = 15.2 \times 10^{-6}$ g cm^{-1} s^{-1}), $T = 1.95$ K (where $\rho_s = 0.07542$ g cm^{-3}, $\rho_n = 0.07012$ g cm^{-3} and $\mu_n = 14.1435 \times 10^{-6}$ g cm^{-1} s^{-1}), and $T = 2.171$ K (where $\rho_s = 0.00652$ g cm^{-3}, $\rho_n = 0.13955$ g cm^{-3} and $\mu_n = 25.40145 \times 10^{-6}$ g cm^{-1} s^{-1})). For the two lowest temperatures, we used two different ring radii: $R = 0.00025$ cm and $R = 0.00125$ cm, whereas for the two larger temperatures, we have studied only the $R = 0.00125$ cm case. This is because for the larger temperatures, the $R = 0.00025$ cm rings were shrinking so fast that (for the initial particle/ring distance mentioned above) collisions were not occurring. In other words, the particle and the ring did not reach a close enough proximity for the latter to become unstable and attach to the spherical surface as was shown in Kivotides *et al.* (2006*a*). Although we have performed computations with zero initial particle velocities, we have also performed a search in velocity space for two cases, i.e. $T = 1.95$ K and $T = 2.171$ K. The particle diameter $2a = 2 \times 10^{-4}$ cm was chosen in agreement with particle sizes used in experiments. All computations reported here were done with this particle size. Moreover, in all cases, the initial particle–vortex distance was $1.5a$. The vortex velocity is directed towards the positive y-axis, and the z-axis is along the vertical direction.

The accuracy of all results presented here was continuously monitored throughout all computations. Since the scope of our method is to enforce the zero radial velocity boundary conditions on the surface of the particle, we have devised an appropriate accuracy criterion. In particular, if the boundary condition were enforced exactly, at all points on the particle's surface the total velocity vector would form a 90° angle with the radial direction vector. We allow small computational deviations from this exact condition only up to a given tolerance from 0.01° to 0.1°. This is achieved with a modest number of terms in the Legendre expansion, of the order of 100. We have

https://doi.org/10.1017/S0022112008001559 Published online by Cambridge University Press

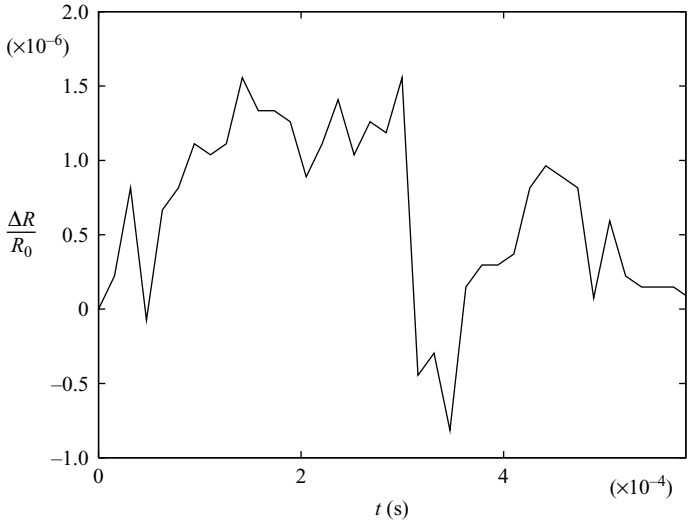


FIGURE 1. Relative error in the vortex-ring radius data $\Delta R/R_0$ versus time. The ring has radius $R_0 = 0.00025$ cm and propagates at $T = 0$ K. There were approximately 3.7×10^4 time steps taken within this time interval.

also verified the accuracy of the purely vortex dynamics algorithms. It is important that the latter enforce the conservation of energy during vortex-ring propagation at zero temperature. In practice, this means that the variations of the ring's diameter and planarity during its motion ought to be negligible. Moreover, these must be true for the actual ring diameters and computational time steps and discretization lengths employed in the particle–vortex computations. Figure 1 shows the relative error $\Delta R/R_0$ in the ring's radius data when a ring of radius $R_0 = 0.00025$ cm propagates at $T = 0$ K over a period of time $\Delta t = 0.0006$ s. There were approximately 3.7×10^4 time steps taken within this time interval. The computational specifications are identical to the corresponding case in the actual results. Evidently, $\Delta R/R_0$ is of order 10^{-6}. Morevover, the maximum deviation from exact planarity (the numerical 'width' of the ring) is 2×10^{-8} cm. The particle radius represents a basic length scale that must be well resolved in order to capture the relevant physics which, as the results indicate, are determined by the formation upon particle–vortex collision of a Kelvin-wave system along the vortex. By choosing a grid size 12 times smaller than the particle diameter, we ensure that particle–Kelvin-wave interactions at the particle scale are captured well. This resolution requirement is met by a discretization length $\delta\ell \approx 1.56 \times 10^{-5}$ cm. The time step δt must not allow the fastest Kelvin wave in the system to propagate by more than one $\delta\ell$ per time step, and must not exceed 0.25τ. Here, the Stokes time τ is given by the formula $\tau = a^2\rho_p/3\mu_n$, where ρ_p is the mass density of the particle and μ_n is the dynamic viscosity of the normal fluid. This time is the characteristic time that viscous forces require in order to damp particle motion in the absence of vortex effects. The purpose of the prefactor 0.25 is to ensure that the viscous damping process is adequately resolved. For particle diameter $2a = 2 \times 10^{-4}$ cm, the three temperature cases $T = 1.3$ K, $T = 1.95$ K and $T = 2.171$ K correspond to $\tau = 3.1935 \times 10^{-5}$ s, $\tau = 3.4301 \times 10^{-5}$ s and $\tau = 1.9170 \times 10^{-5}$ s, respectively. The typical time step is $\delta t \approx 0.15 \times 10^{-7}$ s.

https://doi.org/10.1017/S0022112008001559 Published online by Cambridge University Press

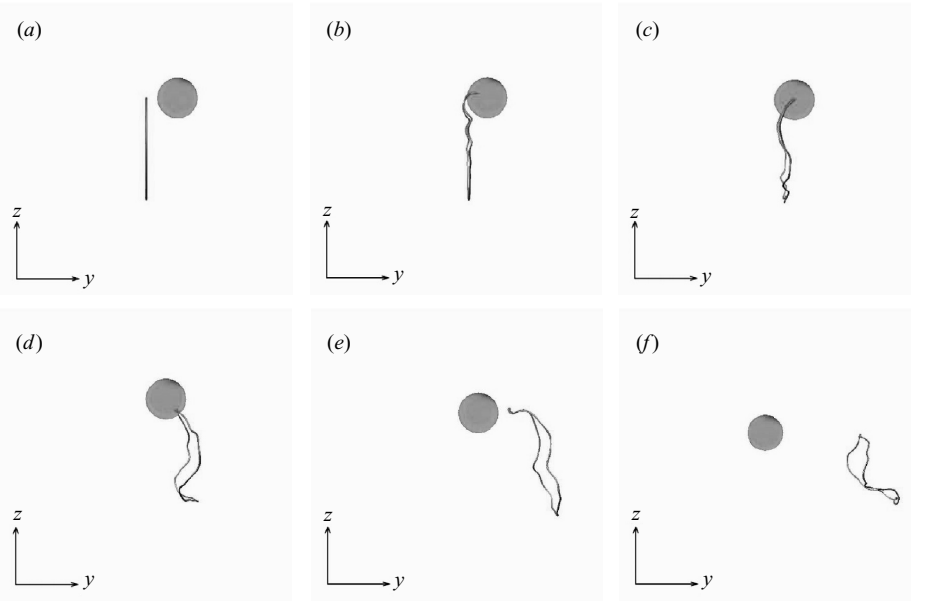


FIGURE 2. Particle–vortex collision for initial particle speed $V = 0$ cm s^{-1}, at $T = 0$ K. The vortex-ring has radius $R = 0.00025$ cm and moves to the right with initial velocity 3.3465 cm s^{-1}. The initial vortex-ring plane is normal to the figure. Time increases as follows: (*a*) $t_1 = 0$ s, (*b*) $t_2 = 0.1892 \times 10^{-6}$ s, (*c*) $t_3 = 0.3154 \times 10^{-6}$ s, (*d*) $t_4 = 0.6940 \times 10^{-5}$ s, (*e*) $t_5 = 0.1640 \times 10^{-4}$ s, (*f*) $t_6 = 0.2208 \times 10^{-4}$ s. As the vortex attaches to the particle, a system of vortex waves develops. The vortex wanders for some time at the back of the particle, before detaching from it.

Finally, in discussing the solutions, we will refer to the various contributions to the total force acting on the particle. These are the boundary-induced force

$$\boldsymbol{f}_b = \tfrac{1}{2}\rho_s \int_S \mathrm{d}S\ (\boldsymbol{V}^s + \boldsymbol{V}^b)^2 \hat{\boldsymbol{n}}, \tag{4.1}$$

the damping force

$$\boldsymbol{f}_d = 6\pi a \mu_n (\boldsymbol{V}^n - \boldsymbol{V}^p), \tag{4.2}$$

and the local force

$$\boldsymbol{f}_l = 2\pi\rho_s a^3 \partial \boldsymbol{V}^s(z,t)/\partial t. \tag{4.3}$$

4.1. *Temperature* $T = 0$ K

The results for the smallest ring case are shown in figure 2. Figure 2(*a*) depicts the initial configuration. The ring is set on a collision course with the particle's centre. Figure 2(*b*) shows that as the ring attaches to the particle, it develops Kelvin waves conceptually similar to the Kelvin-wave cascade in pure superfluid turbulence (Kivotides *et al.* 2001; Nazarenko & West 2003; Vinen, Tsubota & Mitani 2003; Kozik & Svistunov 2004). In figure 2(*c*), the vortex has propagated half-way through the particle's diameter before moving lower and towards the back of the sphere where it wanders for some time, shaking the particle as it moves along its surface (figure 2*d*), before it dettaches from it (figure 2*e*). As vortex and particle drift apart (figure 2*f*), the particle moves essentially in a straight line. The latter is evident in the results of figure 3(*a*), where all components of the particle's velocity become constant

https://doi.org/10.1017/S0022112008001559 Published online by Cambridge University Press

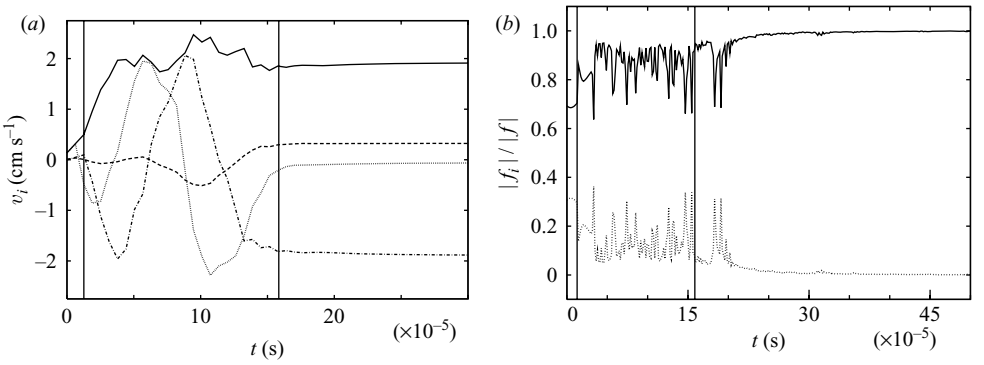


FIGURE 3. Particle–vortex collision for initial particle speed $V = 0$ cm s^{-1}, at $T = 0$ K. The particle's diameter is $2a = 2 \times 10^{-4}$ cm, the ring radius is $R = 0.00025$ cm, and the initial particle–vortex distance is $1.5a$. The solid vertical lines mark the times of particle–vortex collision and separation. (*a*) Particle velocity evolution. The particle oscilates in the y- (dot-dashed line) and z- (dotted line) directions as indicated by the change of the velocity sign along these directions. The dynamics of the x-component (dashed line) are less pronounced. The solid line indicates the total velocity magnitude. After the detachement of the vortex from the particle, the latter moves essentially in a straight line. (*b*) Partial contributions to the total force magnitude. The local force $\boldsymbol{f}_l$ (solid line) dominates over the boundary force $\boldsymbol{f}_b$ (dotted line).

after vortex–particle detachment. Figure 3 also indicates that the forces acting on the particle while it is in contact with the vortex are orders of magnitude stronger than any distant interactions between the vortex and the particle. According to figure 3(*b*), the local force dominates over the boundary-induced force. This is mainly due to the Kelvin-wave system which developed on the vortex during the collision. The results suggest that the introduction of particles in pure superfluid turbulent flow will have a non-trivial effect on the energetics of this flow, via the introduction of Kelvin-wave cascades. The physics of these cascades would be different from the physics of the pure superfluid Kelvin-wave system owing to the presence of the spherical boundary. As is well known from studies of normal-fluid turbulent flows past solid surfaces, the presence of the latter alters the statistical structure of the former.

The solution for the larger ring radius $R = 0.00125$ cm appears in figure 4. It is phenomenologically different from the previous one. As the ring attaches to the particle, the latter starts moving along circular orbits that grow in diameter with time (figure 4*b*,*c*). Figure 5 shows a detail of the (y, z)-plane projection of the particle's centre trajectory after the collision shown in figure 4. Eventually, the particle breaks free from the vortex, not because the vortex is detached from it, but because the loop reconnects with itself allowing the particle to escape having acquired a vortex 'tail' (figure 4*d*). This could be a generic feature of interaction of particles with large vortices at ultra small temperatures, since the collision induces Kelvin waves in the vortex that in turn facilitate a self-reconnection. Why are the two solutions qualitatively different? Certainly the collision velocity plays an important role, since in the small-ring case the vortex moves past the particle without allowing enough time for the latter to accelerate under the influence of the interaction forces. Indeed, the times of figure 2 differ by orders of magnitude from the times of figure 4. Another interpretation, which also agrees with the results of Kivotides *et al.* (2008) at finite temperatures, is that the smaller the particle (relative to the vortex size), the more it tends to be trapped by the colliding vortex. In particular, figure 6(*a*) shows the

https://doi.org/10.1017/S0022112008001559 Published online by Cambridge University Press

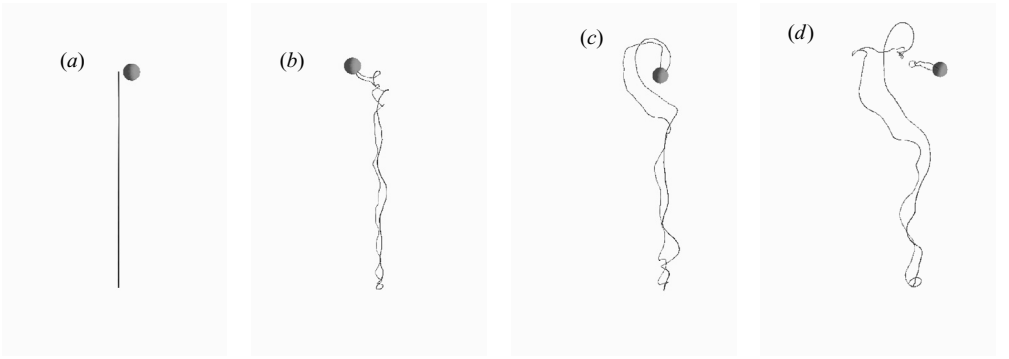


FIGURE 4. Particle–vortex collision for initial particle speed $V = 0$ cm s^{-1}, at $T = 0$ K. The vortex-ring has radius $R = 0.00125$ cm and moves to the right with initial velocity 0.7714 cm s^{-1}. The initial vortex-ring plane is normal to the figure. Time increases as follows: (*a*) $t_1 = 0$ s, (*b*) $t_2 = 0.3407 \times 10^{-3}$ s, (*c*) $t_3 = 0.5679 \times 10^{-3}$ s, (*d*) $t_4 = 0.7698 \times 10^{-3}$ s. The particle spirals out from the point of initial contact, before a self-reconnection of the capturing vortex allows it to escape.

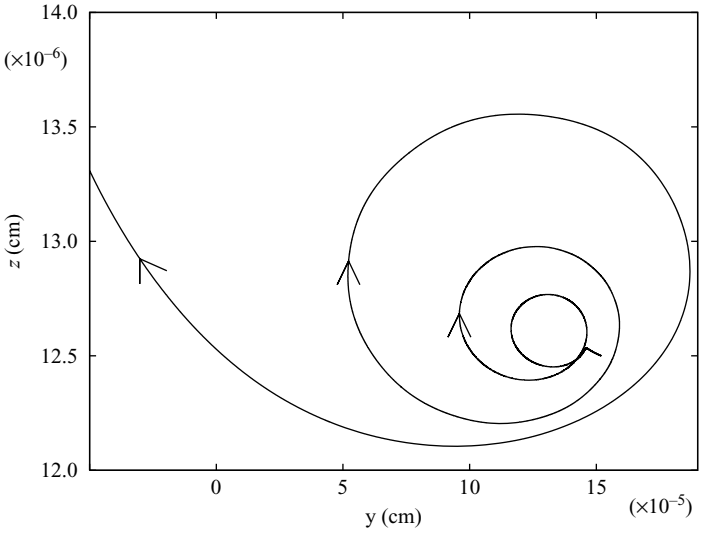


FIGURE 5. Detail of the (y, z)-plane projection of the particle's centre trajectory after the collision shown in figure 4. The arrows indicate the direction of a distinctly spiralling motion. The path shown starts at $t = 0$ s and ends at $t = 0.34 \times 10^{-3}$ s.

particle velocity components. It depicts that, as the particle remains attached to the vortex for longer times, its kinetic energy increases. This is suggestive of a trapping mechanism. As in the smaller-ring case, the particle would like to separate from the vortex. However, when the vortex is large, it tends to efficiently oppose this tendency by turning the particle against its direction of motion. This leads to the outward-spiralling particle trajectories. As the forces acting on the particle change its direction, they also do work on it and increase its kinetic energy. Since all superfluid vortices have the same circulation, larger rings correspond to larger fluid kinetic energies that act as reservoirs of available particle kinetic energy. The higher the trapping capacity of a vortex, the higher the kinetic energy that the particle acquires during its interaction with it.

https://doi.org/10.1017/S0022112008001559 Published online by Cambridge University Press

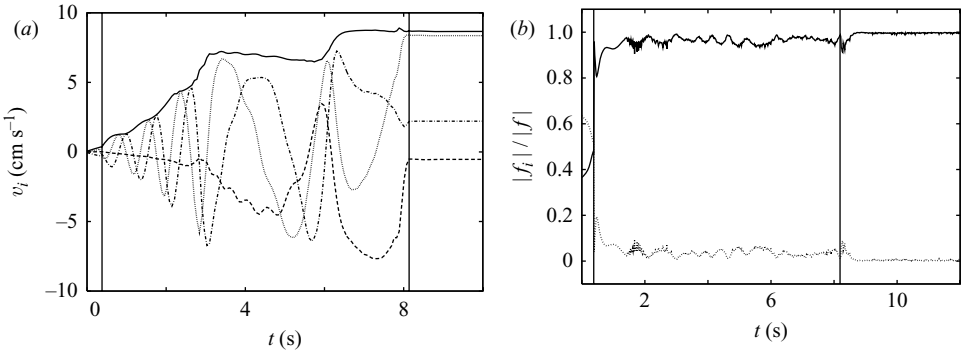


FIGURE 6. Particle–vortex collision for initial particle speed $V = 0$ cm s^{-1}, at $T = 0$ K. The particle's diameter is $2a = 2 \times 10^{-4}$ cm, the ring radius is $R = 0.00125$ cm, and the initial particle–vortex distance is $1.5a$. The solid vertical lines mark the time of particle–vortex collision and separation. (*a*) Particle velocity evolution. There are rapid variations of the y-component (dot-dashed line)and z-component (dotted line) of the velocity, that correspond to the spiralling particle motion on the (y, z)-plane. The dynamics of the x-component (dashed line) are less pronounced yet more interesting than in the corresponding figure 3. The solid line indicates the total velocity magnitude. (*b*) Partial contributions to the total force magnitude. With the exception of pre-collision times, the local force $\boldsymbol{f}_l$ (solid line) dominates over the boundary force $\boldsymbol{f}_b$ (dotted line). This is due to the system of Kelvin waves that develops on the vortex upon collision.

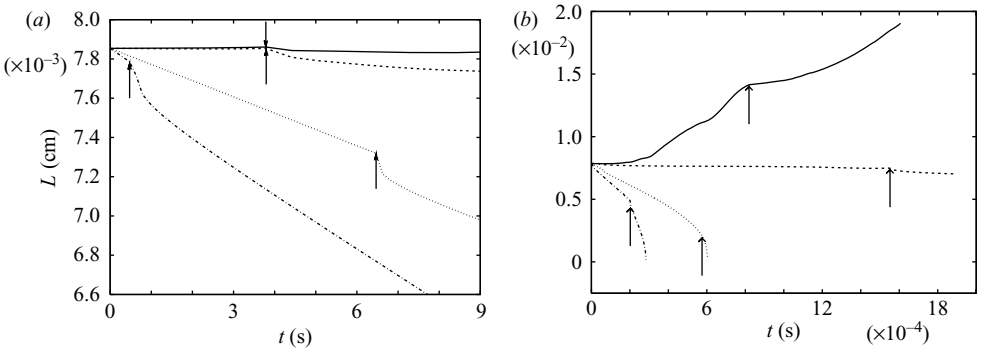


FIGURE 7. Comparison of vortex-ring length evolution for the initial ring radius $R = 0.00125$ cm case. Line sare: $T = 0$ K (solid), $T = 1.3$ K (dashed), $T = 1.95$ K (dotted) and $T = 2.171$ K (dot-dashed). (*a*) Vortex-ring length for small times. The arrows mark the points where the loop attaches to the particle. (*b*) Vortex-ring length for all computation times. The arrows mark the points where the loop detaches from the particle.

Figure 7 shows the evolution of the vortex loop length (solid lines). The almost constant loop length until the onset of collision is plausible, since at this temperature there are no mutual friction effects, and, in addition, previous work (Schwarz 1985; Kivotides *et al.* 2006*a*) has shown that the vortex is being deformed by the particle only during the very late stages of its approach to it. Notice that the vortex length increases even after the particle and the vortex separate from each other.

4.2. *Temperature* $T = 1.3$ K

The evolution of the system's configuration for temperature $T = 1.3$ K is shown in figure 8. Although mutual friction damps the collision-induced Kelvin waves, the

https://doi.org/10.1017/S0022112008001559 Published online by Cambridge University Press

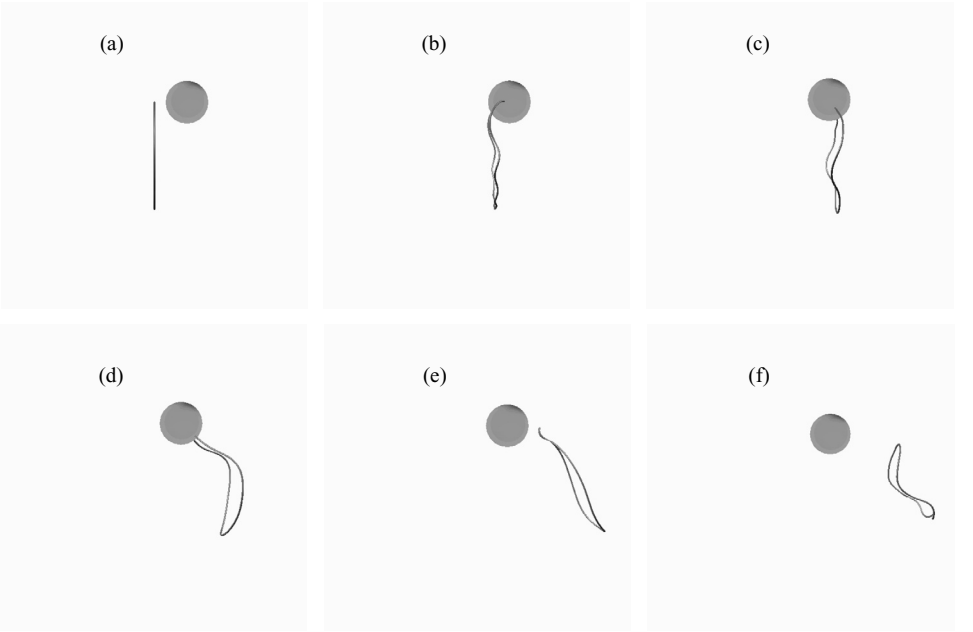


FIGURE 8. Particle–vortex collision for initial particle speed $V = 0$ cm s^{-1}, at $T = 1.3$ K. The vortex-ring has radius $R = 0.00025$ cm and moves to the right with initial velocity 3.4346 cm s^{-1}. The initial vortex-ring plane is normal to the figure. Time increases as follows: (*a*) $t_1 = 0$ s, (*b*) $t_2 = 0.2524 \times 10^{-4}$ s, (*c*) $t_3 = 0.5048 \times 10^{-4}$ s, (*d*) $t_4 = 0.1073 \times 10^{-3}$ s, (*e*) $t_5 = 0.1514 \times 10^{-3}$ s, (*f*) $t_6 = 0.1704 \times 10^{-3}$ s. The trajectory of the loop is similar to the corresponding $T = 0$ K case (figure 2). However, there are differences, such as for example the mutual friction-induced loop smoothness.

loop's trajectory is similar to that in the corresponding $T = 0$ K case. Figure 9(*a*) shows the various components of the particle velocity, and figure 9(*b*) shows the partial contributions to the total force acting on the particle. The local and boundary forces dominate between particle–vortex collision and separation. After detachment, in contrast to the $T = 0$ K case, the particle dynamics is determined mainly by the viscous drag force, and the particle is brought to a halt.

Figure 10 shows the system's configuration for the $R = 0.00125$ cm case. Mutual friction damps the collision-induced Kelvin waves, and, in a sense, the vortex is tethered at its upper end by the particle. Since the lower vortex part is not strongly affected by the collision, it continues its motion creating a stretched bridge that connects the vortex with the particle. When this bridge becomes too narrow, the vortex reconnects with itself and separates from the particle.

Figure 11 shows the evolutions of velocity (figure 11*a*) and partial force contributions (figure 11*b*). As expected, the velocity magnitudes are smaller than those of the $T = 0$ K case. The force data suggest that the decisive factor for the dynamics is the development and evolution of Kelvin waves upon particle–vortex collision. When $T = 0$ K, these are allowed to evolve, and lead to a large local force which is mainly responsible for the vortex-trapping potential. When $T = 1.3$ K, mutual friction damps these waves and the dynamics are dominated by the boundary force. This state of balance between the forces, however, leads to very different system evolutions.

Figure 7 shows the vortex length evolution (dashed lines). Although the collision happens at almost the same time as the collision in the $T = 0$ K case, vortex-wave

https://doi.org/10.1017/S0022112008001559 Published online by Cambridge University Press

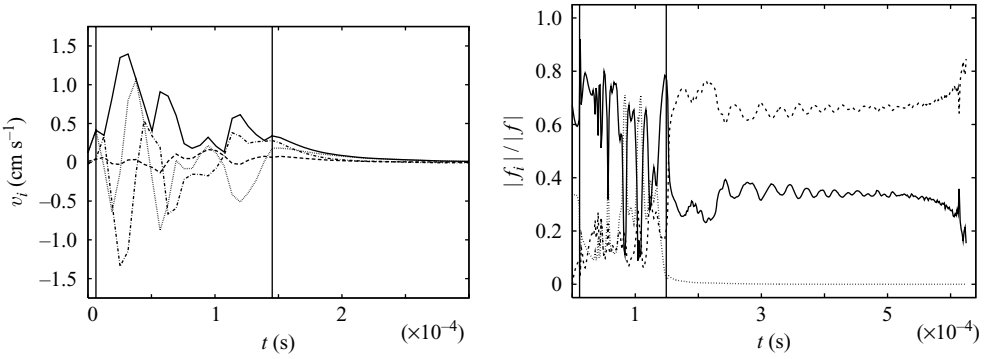


FIGURE 9. Particle–vortex collision for initial particle speed $V = 0$ cm s^{-1}, at $T = 1.3$ K. The particle's diameter is $2a = 2 \times 10^{-4}$ cm, the ring radius is $R = 0.00025$ cm, and the initial particle–vortex distance is $1.5a$. The solid vertical lines mark the time of particle–vortex collision and separation. (*a*) Particle velocity evolution. The dashed line signifies the x-component, the dot-dashed line corresponds to the y-component, and the z-component is depicted by the dotted line. The solid line indicates the total velocity magnitude. Even after loop detachement, in contrast to the $T = 0$ K case, there are some residual velocity dynamics, since the Stokes drag tends to reduce the particle velocity to zero. (*b*) Partial contributions to the total force magnitude. As long as the vortex is attached to the sphere, the most dominant forces are the local (solid line) and boundary force (dotted line); after loop–particle separation, the drag force (dashed line) dominates, and reduces the particle velocity.

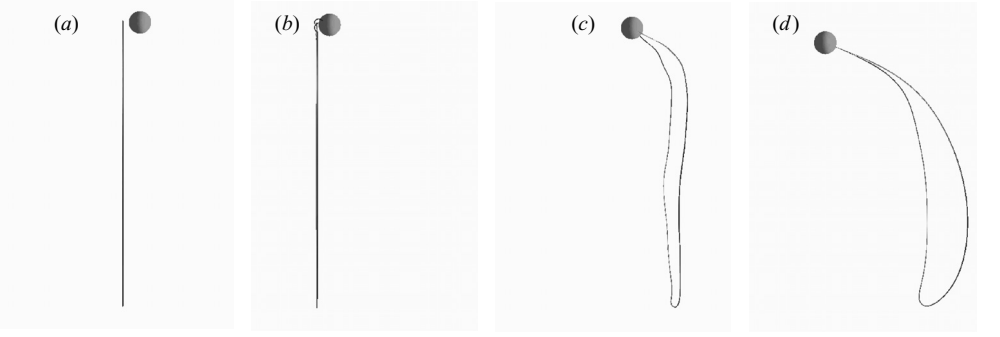


FIGURE 10. Particle–vortex collision for initial particle speed $V = 0$ cm s^{-1}, at $T = 1.3$ K. The vortex-ring has radius $R = 0.00125$ cm and moves to the right with initial velocity 0.7868 cm s^{-1}. The initial vortex-ring plane is normal to the figure. Time increases as follows: (*a*) $t_1 = 0$ s, (*b*) $t_2 = 0.4417 \times 10^{-4}$ s, (*c*) $t_3 = 0.5931 \times 10^{-3}$ s, (*d*) $t_4 = 0.1317 \times 10^{-2}$ s. In opposition to the $T = 1.3$ K, $R = 0.00025$ cm case, the system's phenomenology here is very different from the corresponding $T = 0$ K case. The loop remains smooth and its lower part is not much affected by the collision. As a result, a stretched bridge is created between the main loop and the particle. Evidently, mutual friction, by smoothing out the Kelvin waves on the vortex, neutralizes the trapping effects of the local force, and in conjunction with the viscous drag, damps the spiralling particle trajectory of the corresponding $T = 0$ K case.

damping leads to a much smaller (and in fact monotonically decreasing) vortex length, as well as to a longer period of particle–vortex contact. The rate of length reduction is small, and so the $T = 1.3$ K case is an important boundary between the length-increasing $T = 0$ K evolutions, and the predominantly length-decreasing higher-temperature cases that we are going to examine next.

https://doi.org/10.1017/S0022112008001559 Published online by Cambridge University Press

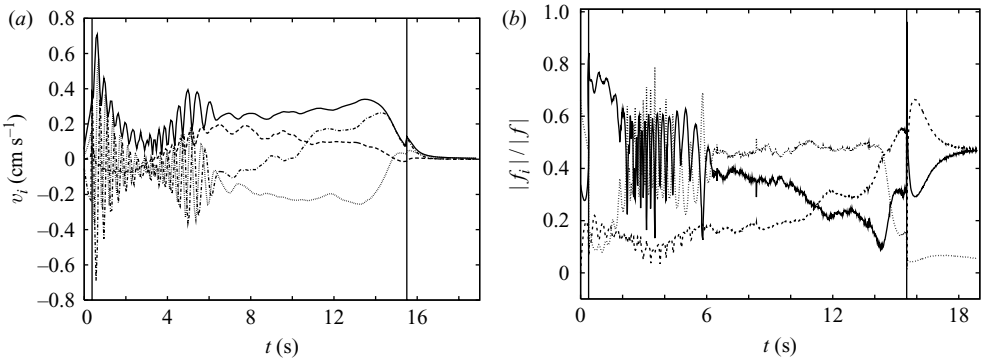


FIGURE 11. Particle–vortex collision for initial particle speed $V = 0$ cm s^{-1}, at $T = 1.3$ K. The particle's diameter is $2a = 2 \times 10^{-4}$ cm, the ring radius is $R = 0.00125$ cm, and the initial particle–vortex distance is $1.5a$. The solid vertical lines mark the times of particle–vortex collision and separation. (*a*) Particle velocity evolution. The shaking of the particle by the vortex is illustrated by the oscillations of the velocity along the y- (dot-dashed line) and z-directions (dotted line). The solid line signifies the total velocity magnitude, and the dashed line is the x-component of velocity. (*b*) Partial contributions to the total force magnitude. The local force (solid line) is dominant immediately after the collision. Its importance decays with time, as the mutual friction smooths the vortex contour, and the boundary force (dotted line) becomes the dominant one. Viscous drag (dashed line) has a small influence on the dynamics in between the collision and separation times, but eventually becomes the dominant force.

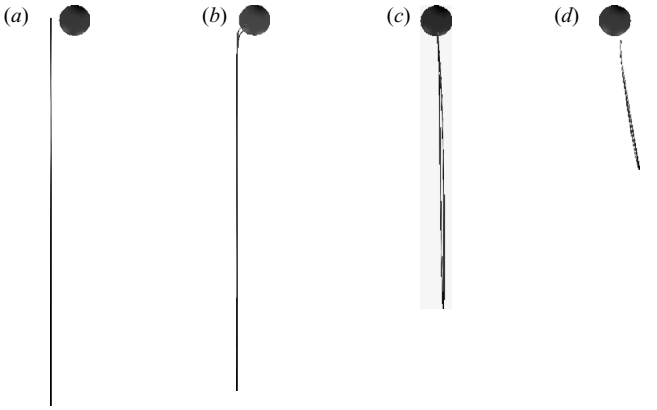


FIGURE 12. Particle–vortex collision for initial particle speed $V = 0$ cm s^{-1}, at $T = 1.95$ K. The vortex-ring has radius $R = 0.00125$ cm and moves to the right with initial velocity 0.2725 cm s^{-1}. The initial vortex-ring plane is normal to the figure. Time increases as follows: (*a*) $t_1 = 0$ s, (*b*) $t_2 = 0.6941 \times 10^{-4}$ s, (*c*) $t_3 = 0.3723 \times 10^{-3}$ s, (*d*) $t_4 = 0.5805 \times 10^{-3}$ s. The particle shrinks much faster than in the $T = 1.3$ K case, and so it has to travel a longer distance before it collides with the particle, (*b*). While attached to the particle (*c*), the vortex shrinks significantly. Since the upper vortex part is tethered by the particle, it tends to be stretched by the lower part that continues its forward motion. This effect eventually causes particle–vortex detachment, (*d*), by inducing a self-reconnection between the segments of the stretched bridge.

4.3. *Temperature* $T = 1.95$ K

Figure 12 shows the particle–vortex configuration. As shown in figure 7 (dotted lines) the vortex collides with the particle at a later time than in the $T = 1.3$ K case (dashed lines). This at first seems to be a paradox, since the mutual friction-induced increased rate of ring-radius reduction would lead us to expect that the vortex would move faster

https://doi.org/10.1017/S0022112008001559 Published online by Cambridge University Press

than in the $T = 1.3$ K case, and collide with the particle at earlier times. However, we must also take into account that, since the particle moves on a steady horizontal plane, the tip of the vortex will shrink below this plane and the vortex must cover a larger distance before collision (figure 12*b*). This effect is depicted in the results of figure 7 (dotted lines). After collision, the mutual friction causes the vortex to shrink rapidly while still remaining attached to the particle (figure 12*c*), before detaching from it (figure 12*d*). In order to study the effect of initial particle velocity on the system's dynamics, we have performed computations for the $T = 1.95$ K, $R = 0.00125$ cm case with initial particle speeds $V = -10$ cm s^{-1} and $V = -25$ cm s^{-1}. The loop-length results for these cases (including the $T = 2.171$ K, $V = 0$ cm s^{-1} data for comparison) are shown in figure 13. The results show that, as the initial velocity is increased in the $T = 1.95$ K case, the particle attaches to the sphere much earlier than for the $T = 2.171$ K, $V = 0$ cm s^{-1} case. Moreover, although for $V = -10$ cm s^{-1} the initial velocity effect is not strong enough to differentiate strongly the vortex length dynamics from their zero initial-velocity counterparts, there is an obvious effect for $V = -25$ cm s^{-1}. For this case, figure 14 indicates that, throughout the system's evolution, the lower part of the vortex is unaffected by its collision with the particle, and only its upper part is stretched by the particle upon detachement. This stretching is responsible for the increase of vortex length observed in figure 13. Overall, the ratio between particle–vortex contact time scale and mutual friction action time scale is an important dynamical factor at these high temperatures.

The results for the particle velocity and the particle forces are shown in figure 15. Figure 15(*b*) indicates that the superfluid-induced forces dominate the dynamics throughout the period of particle–vortex contact. The normal-fluid-induced viscous drag becomes important only around the onset of detachment. This is because the ring has shrunk drastically by the time of detachment, and in fact disappears completely immediately after. The latter explains why the superfluid-induced forces drop sharply to zero at $t = 0.000604$ s. Both the y- and z-components of the particle velocity become negative before the onset of collision (figure 15*b*). This behaviour is explained by noticing that the vortex initially moves with its velocity pointing toward the positive y-axis, and at the same time (as shown in figure 12), shrinks toward the negative z-axis. Thus, the particle, since it is attracted by the vortex and tends to move towards it, develops negative velocity components along the y- and z-axes. Upon collision, a low pressure develops in the area of particle vortex contact, and the resulting force rapidly pushes the particle along the negative y-axis. However, the viscous drag force, which is strong around collision time, strives to bring the particle to a halt, and so the post-collisional y-velocity tends subsequently towards positive values. In accord with these, notice that a plateau in the graph of the y-velocity is associated with domination of the viscous force by the superfluid-induced forces, and that further non-trivial dynamics are possible only towards detachment, when the balance of forces is adjusted once again.

4.4. *Temperature* $T = 2.171$ K

Figure 16 shows the time evolution of the system's configuration. According to figure 7 (dot-dashed lines), the particle–vortex collision (figure 16*b*) happens at an earlier time than for the $T = 1.95$ K case (dotted lines). This is because, owing to enhanced mutual friction action at this high temperature, the ring-radius shrinks at a dramatic rate and accelerates accordingly. Moreover (figure 7), it is remarkable that despite the higher temperature, at the time of detachment (figure 16*d*), the ring has shrunk less than at the corresponding $T = 1.95$ K case separation time. This is because, owing to

https://doi.org/10.1017/S0022112008001559 Published online by Cambridge University Press

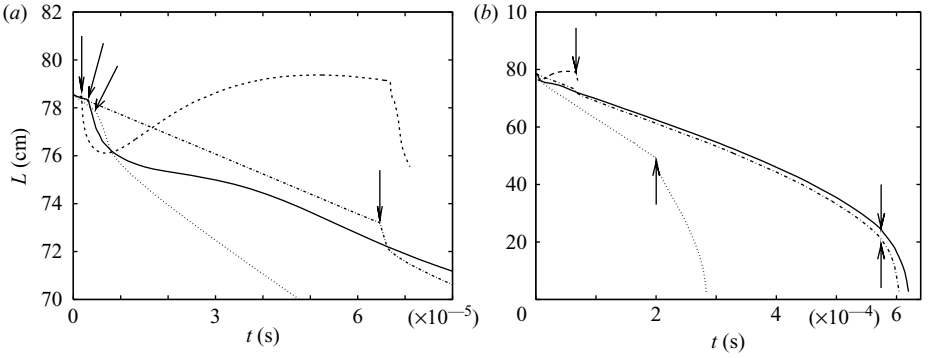


FIGURE 13. Comparison of initial vortex-ring length evolution for radius $R = 0.00125$ cm. Lines are: $T = 1.95$ K, $V = 0$ cm s^{-1} (dot-dashed), $T = 1.95$ K, $V = -10$ cm s^{-1} (solid), $T = 1.95$ K, $V = -25$ cm s^{-1} (dashed) and $T = 2.171$ K, $V = 0$ cm s^{-1} (dotted). (*a*) Vortex-ring length for small times. The arrows mark the points where the loop attaches to the particle. (*b*) Vortex-ring length for all computation times. The arrows mark the points where the loop detaches from the particle.

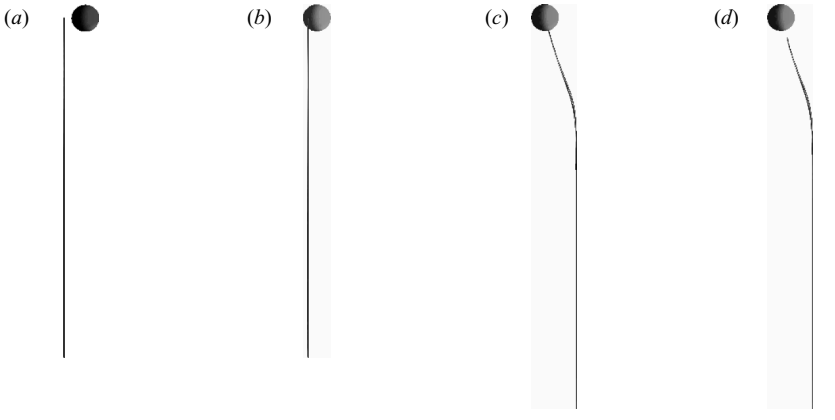


FIGURE 14. Particle–vortex collision for initial particle speed $V = -25$ cm s^{-1}, at $T = 1.95$ K. The vortex-ring has radius $R = 0.00125$ cm and moves to the right with initial velocity 0.3047 cm s^{-1}. The initial vortex-ring plane is normal to the figure. Time increases as follows: (*a*) $t_1 = 0$ s, (*b*) $t_2 = 0.3786 \times 10^{-5}$ s, (*c*) $t_3 = 0.6562 \times 10^{-4}$ s, (*d*) $t_4 = 0.6814 \times 10^{-4}$ s. The effect of initial velocity becomes clear when we compare with the results of figure 12. The ring spends a small amount of time in contact with the particle, and has scarcely shrunk upon detachment.

its higher velocity (because of higher shrinking rate) relative to the $T = 1.95$ K case, the ring does not stay in contact with the particle for a long time, and so mutual friction does not have enough time to act.

For this case too, we have performed a series of computations in order to investigate the effects of initial particle velocity. It was found that, as the initial velocity increases, the vortex is vigorously deformed as it tries to avoid the approaching particle. This process is active at all temperatures, but it is more pronounced at $T = 2.171$ K owing to higher values of the mutual friction coefficients. Figure 17 demonstrates the deformation mechanism for initial velocity $V = -1000$ cm s^{-1}. As the vortex and the particle approach each other (figure 17*a*), the vortex is deformed into an arc that tends to avoid the particle (figure 17*b*,*c*). However, at the points where

https://doi.org/10.1017/S0022112008001559 Published online by Cambridge University Press

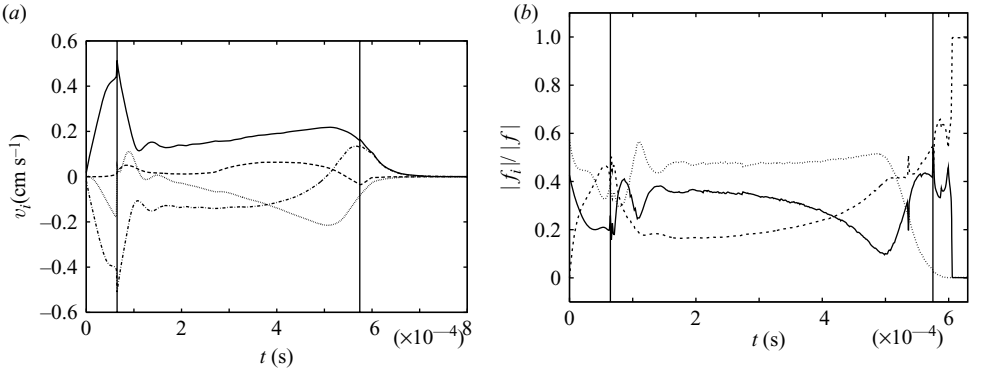


FIGURE 15. Particle–vortex collision for initial particle speed $V = 0$ cm s^{-1}, at $T = 1.95$ K. The particle's diameter is $2a = 2 \times 10^{-4}$ cm, the ring radius is $R = 0.00125$ cm, and the initial particle–vortex distance is $1.5a$. The solid vertical lines mark the times of particle–vortex collision and separation. (*a*) Particle velocity evolution. The dashed line signifies the x-component, the dot-dashed line corresponds to the y-component, and the z-component is depicted by the dotted line. The solid line indicates the total velocity magnitude. The particle is sharply pushed along the negative y-axis upon collision, and the effects of this forcing are subsequently damped by viscous drag effects. (*b*) Partial contributions to the total force magnitude. The lines signify the local force (solid), the boundary-induced force (dotted) and the viscous drag force (dashed). The superfluid-induced forces dominate the dynamics throughout the period of particle–vortex contact.

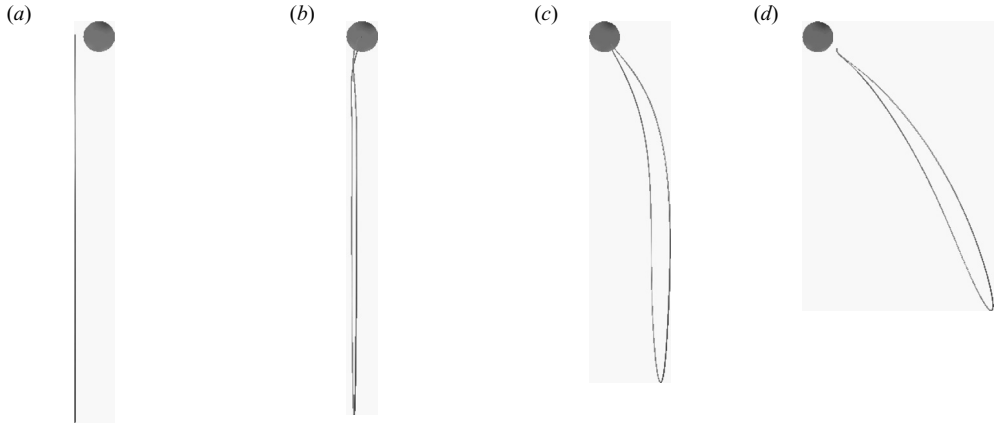


FIGURE 16. Particle–vortex collision for initial particle speed $V = 0$ cm s^{-1}, at $T = 2.171$ K. The vortex-ring has radius $R = 0.00125$ cm and moves to the right with initial velocity 4.7225 cm s^{-1}. The initial vortex-ring plane is normal to the figure. Time increases as follows: (*a*) $t_1 = 0$ s, (*b*) $t_2 = 0.1893 \times 10^{-4}$ s, (*c*) $t_3 = 0.9622 \times 10^{-4}$ s, (*d*) $t_4 = 0.2033 \times 10^{-3}$ s.

the arc meets the (relatively) undisturbed part of the vortex, the vortex curvature is high and increases proportionally to the growth of the arc radius. At the points of this increased curvature, the local vortex velocity becomes very high, and so the vortex rapidly collapses onto the particle, as indicated by the arrows of figure 17(*d*). After the collision (figure 17*e*), the particle acquires a vortex handle (figure 17*f*). This intriguing phenomenon begs the question of whether there is a threshold velocity above which the vortex avoids the particle. In order to answer this question, we have

https://doi.org/10.1017/S0022112008001559 Published online by Cambridge University Press

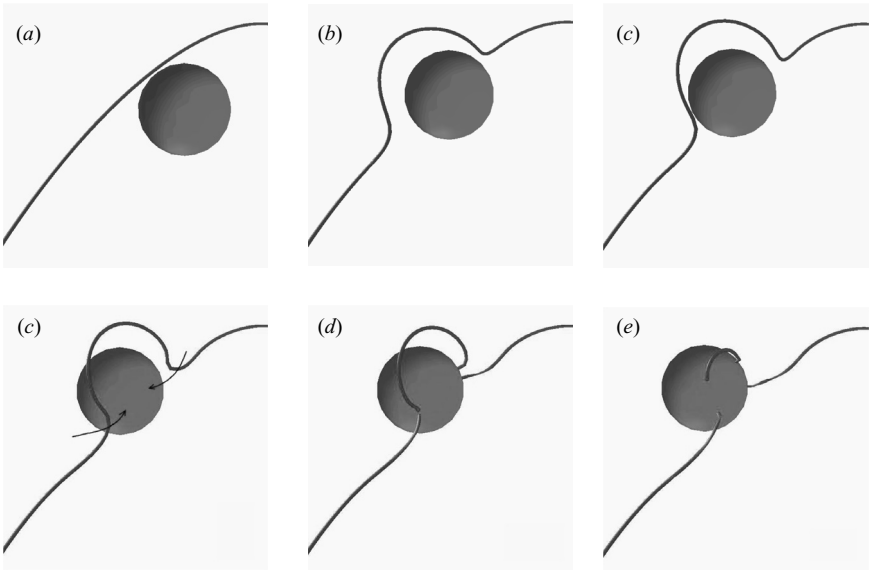


FIGURE 17. Particle–vortex collision for initial particle speed $V = -1000$ cm s^{-1}, at $T = 2.171$ K. The vortex-ring has radius $R = 0.00125$ cm and moves to the right with initial velocity 42.3787 cm s^{-1}. For clarity, only part of the vortex loop is shown. Time increases from as follows: (*a*) $t_1 = 0$ s, (*b*) $t_2 = 0.1059 \times 10^{-6}$ s, (*c*) $t_3 = 0.1414 \times 10^{-6}$ s, (*d*) $t_4 = 0.1750 \times 10^{-6}$ s, (*e*) $t_5 = 0.1888 \times 10^{-6}$ s, (*f*) $t_6 = 0.2226 \times 10^{-6}$ s. As the particle-ring approach deforms the latter, the high-curvature loop segments formed at the roots of the induced vortex arc cause the loop to collapse upon the particle forming a handle.

gradually increased the initial particle velocity. We found that even up to speeds of $V = -10\,000$ cm s^{-1}, the vortex always collides with the particle.

The results for the particle forces and particle velocities for speed $V = 0$ cm s^{-1} are shown in figure 18. Figure 18(*a*) suggests that upon collision, the particle is sharply pushed along the leftward-downward direction. This forcing is due to the pressure difference between the low-pressure area formed by vortex–particle contact and the pressure on the upper hemisphere of the particle. Subsequently, this perturbation is strongly damped and there are no particle oscillations. The increased mutual friction effects reduce the impact of the local force immediately after the collision, and Stokes damping becomes the most significant particle force. Notice the differences with the $T = 1.95$ K case (figure 15). They are due to aforementioned differences in the location (along the particle surface) and timing of the collision in the two cases. Because of the particular vortex–particle configuration shown in figure 16(*c*), a low-pressure area is induced on the right particle hemisphere close to particle–vortex detachment. The resulting pressure difference is responsible for the observed positive particle velocity component along the *y*-direction.

5. Conclusion

We have performed self-consistent computations of the interactions between a superfluid vortex ring and a solid particle for two different ring sizes and over a wide range of temperatures starting from absolute zero and ending close to the superfluid transition temperature. At non-zero temperatures, we have kinematically prescribed a motionless normal-fluid component. The ratio of vortex-ring radius over the particle

https://doi.org/10.1017/S0022112008001559 Published online by Cambridge University Press

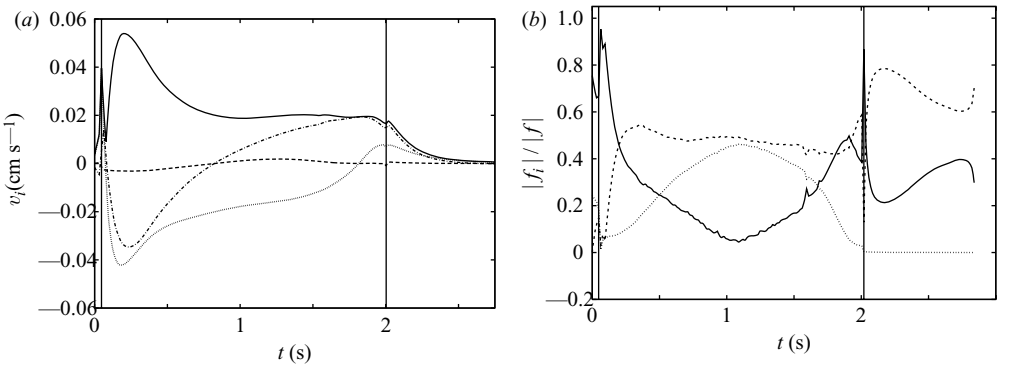


FIGURE 18. Particle–vortex collision for initial particle speed $V = 0$ cm s^{-1}, at $T = 2.171$ K. The particle's diameter is $2a = 2 \times 10^{-4}$ cm, the ring radius is $R = 0.00125$ cm, and the initial particle–vortex distance is $1.5a$. The solid vertical lines mark the times of particle–vortex collision and separation. (*a*) Particle velocity evolution. The dashed line signifies the x-component, the dot-dashed line corresponds to the y-component, and the z-component is depicted by the dotted line. The solid line indicates the total velocity magnitude. After a strong push in the downward-leftward direction upon collision, viscous drag action damps the particle's motion. Close to detachment, the y-velocity acquires positive values. This is due to the particular vortex–particle configuration of figure 16(*c*), which induces a low pressure area on the right particle hemisphere pushing the particle to the right. (*b*) Partial contributions to the total force magnitude. The lines signify the local force (solid), the boundary-induced force (dotted) and the viscous drag force (dashed). During most of the particle–vortex contact period, the particle dynamics are governed by the competition between boundary and viscous forces.

radius was $R/a = 2.5$ for the smaller-ring case, and $R/a = 12.5$ for the larger-ring case. We have found that, in all cases, the particle and the vortex eventually separate.

For $T = 0$ K, larger rings tend to trap the particles more effectively than smaller rings. Owing to the absence of mutual friction effects, the rings are vigorously distorted by the collision-induced Kelvin waves, and lose their ring-like appearance. The $T = 0$ K results also suggest that an experiment monitoring the motion of solid particles in a superfluid vortex link could detect particle–vortex interactions by recording the spiral-like particle motions depicted in figure 4. The larger the rings involved in the process are, the more evident the particle motions would be, since larger rings are more effective than smaller rings in their efforts to trap particles. As indicated by the data, the larger ring induces much higher post-collisional particle velocities than does the smaller ring. Moreover, because of the undamped collision induced vortex wave system, the local force grossly overpowers the boundary force.

For $T > 0$ K, the particle vibrates normal to its direction of motion upon its collision with the vortex. The solutions suggest that smaller rings induce larger vibration velocities. This is exactly opposite to what happens in the $T = 0$ K case, and suggests that, for $T > 0$ K, smaller rings might be easier to detect experimentally. At smaller temperatures (here $T = 1.3$ K and $T = 1.95$ K), the superfluid-induced forces dominate the normal-fluid-induced viscous damping between collision and detachment. As the temperature increases, the increased mutual friction damping of vortex waves (which are the main contributors to the local force) leads to the damping of both the intensity and frequency of post-collision particle vibrations. Overall, as the temperature increases, the importance of the local force is reduced and that of the drag force is increased. This also helps to damp the particle oscillations. In fact, at $T = 2.171$ K, the viscous force is the largest contributor to particle dynamics

https://doi.org/10.1017/S0022112008001559 Published online by Cambridge University Press

between collision and detachment. With the exception of $T = 0$ K, the boundary force is always an important dynamical factor. According to the $T = 1.3$ K data, the collision of particles with vortices would result in sudden particle vibrations (as indicated by the particle velocity data) that could be detected if the vortex system were dilute enough for the particles to move relatively smoothly (i.e. without fluctuations) in between their collisions with the superfluid vortices. The latter is conditional upon the type and energy level of the corresponding normal-fluid flow. We could imagine, for example, a turbulent normal-fluid component. For this case, Kivotides *et al.* (2007*a*) showed that a solid particle would, most of the time, sharply change its direction upon encountering a normal-fluid filament, but, sporadically, also briefly spiral around it. These motions are different from the normal to the particle's direction of motion vibrations depicted here, so, in principle, the effects of the two fluids on the particles could be discernible. In the case of turbulent normal fluid, one possibility concerns the presence of the coherent superfluid bundles calculated in Kivotides (2006). In particular, according to the present results, when a superfluid vortex arc that is curved at the scale of the particle collides with the latter, the two will separate after their interaction. In contrast, for vortices that appear as straight lines at the scale of a particle, Kivotides *et al.* (2008) have shown that, for each $T > 0$ K, there is a corresponding range of incoming particle velocities for which particle and vortex stay together after collision. With respect to this, note also that Kivotides (2005) has shown that, for $T = 1.3$ K, a tangle of superfluid vortices interacting with (a stationary, on the average) normal fluid presents a scaling regime in the histogram of the local vortex curvature, and that the cutoff of this regime is $R_c \approx 10^{-5}$ m. This curvature radius coincides with the radius of the larger ring computed here. In this context, Kivotides (2006) has shown that, in turbulent liquid helium, the normal fluid might induce stretched vortex-bundles of macroscopic circulation in the superfluid. When a solid particle collides with such a bundle of vortices, it might be trapped by them by having its kinetic energy radiated from the point of collision via vortex waves propagating along the bundle. This in turn, in combination with the results of Kivotides (2007), suggests that the induced Kelvin waves, for sufficiently high particle kinetic energy, could excite bundle instability modes that would lead to the destruction of the superfluid coherent structures. In order to address such crucial issues, a combined action of experiment and theory is required.

It is important to note that in our computations we assume that the particle is a perfect sphere, hence we ignore any surface roughness at the vortex core scale. There are two reasons behind this assumption. First, the mathematical method that computes the effect of the particle boundary on the vortices is valid only when the former is a perfect sphere. This is because the spherical shape allows the derivation of an analytical formula for the effect of the boundary on a linear vortex segment which is one of the main results upon which the present computations are based. Secondly, the introduction of small-scale roughness requires a similar refinement of the discretization length along the vortices, which is not computationally feasible. The employed grid is already computationally demanding, and it only resolves adequately the sphere-radius scale phenomena. Having said this, we do not expect the qualitative conclusions of this study to be altered by the inclusion of fine-scale dynamics. The eventual particle–vortex detachment is due to the large-scale velocity of the ring relative to the particle which is determined by the initial ring-radius. Moreover, the relative importance of the contributions of the various forces to particle dynamics depends mostly on the establishment upon collision of a (well-resolved at the particle-radius scale) Kelvin-wave system on the vortices, and not on the wavenumber-space extension

https://doi.org/10.1017/S0022112008001559 Published online by Cambridge University Press

of the spectrum of this system. Finally, another important assumption is that of a kinematically prescribed stationary normal-fluid velocity field. This assumption could be relaxed by developing methods for the calculation of self-consistent interactions between the three fields comprising multiphase liquid helium physics: superfluid, normal-fluid and particulate-solid. This requires (in addition to the methods employed here), the computation of the normal-fluid flow around a suspension of spherical particles. At present, we can only speculate about the physics of such complex interactions. It is well known (Kivotides, Barenghi & Samuels 2000), that a superfluid vortex ring moving in an initially at rest normal fluid generates two normal-fluid vortices around it. Thus, when the superfluid vortex ring collides with the particle, it is as if two normal-fluid vortices also collide with the particle. Moreover, the normal flow around the particle would deform the vortex-ring contour even before collision. For small Reynolds number, creeping normal flow around the particle, the above effects might not be very important, but for higher particle velocities there could be a significant effect that deserves systematic study. Overall, the future development of fully dynamic self-consistent methods would allow a lively interaction between experiment and theory in liquid helium, which could help advance our understanding of these remarkable systems.

This paper is dedicated to the memory of Brian Jackson.

REFERENCES

Barenghi, C. F., Donnelly, R. J. & Vinen, W. F. 1983 Friction on quantized vortices in He II . A review. *J. Low Temp. Phys.* **52**, 189.

Barenghi, C. F., Donnelly, R. J. & Vinen, W. F. 2001 *Quantized Vortex Dynamics and Superfluid Turbulence*. Springer.

Bewley, G. P., Lathrop, D. P. & Sreenivasan, K. R. 2006 Superfluid helium: visualization of quantized vortices. *Nature* **44**, 588.

Brennen, C. E. 2005 *Fundamentals of Multiphase Flow*. Cambridge University Press.

Celik, D. & VanSciver, S. W. 2002 Tracer particle generation in superfluid helium through cryogenic liquid injection for particle image velocimetry (PIV) applications. *Exp. Thermal Fluid Sci.* **26**, 971–975.

Crowe, C. T., Sommerfeld, M. S. & Tsuji, Y. 1998 *Multiphase Flows with Droplets and Particles*. CRC Press, Boca Raton.

Donnelly, R. J. 1991 *Quantised Vortices In Helium II*. Cambridge University Press.

Donnelly, R. J., Karpetis, A. N., Niemela, J. J., Sreenivasan, K. R., Vinen, W. F. & White, C. M. 2002 The use of particle image velocimetry in the study of turbulence in liquid helium. *J. Low Temp. Phys.* **126**, 327–332.

Drew, D. A. & Passman, S. L. 1998 *Theory of Multicomponent Fluids*. Springer.

Finne, A. P., Eltsov, V. B., Hanninen, R., Kopnin, N. B., Kopu, J., Krusius, M., Tsubota, M. & Volovik, G. E. 2006 Dynamics of vortices and interfaces in superfluid ^{3}He. *Rep. Prog. Phys.* **69**, 3157–3230.

Kivotides, D. 2005 Turbulence without inertia in thermally excited superfluids. *Phys. Lett.* A **341**, 193–197.

Kivotides, D. 2006 Coherent structure formation in turbulent thermal superfluids. *Phys. Rev. Lett.* **96**, 175301.

Kivotides, D. 2007 Relaxation of superfluid vortex bundles via energy transfer to the normal fluid. *Phys. Rev.* B **76**, 054503.

Kivotides, D., Barenghi, C. F. & Samuels, D. C. 2000 Triple vortex ring structure in superfluid helium II. *Science* **290**, 777.

Kivotides, D., Vassilicos, J. C., Samuels, D. C. & Barenghi, C. F. 2001 Kelvin waves cascade in superfluid turbulence. *Phys. Rev. Lett.* **86**, 3080.

https://doi.org/10.1017/S0022112008001559 Published online by Cambridge University Press

Kivotides, D., Barenghi, C. F. & Sergeev, Y. A. 2005 Measurement of the normal fluid velocity in superfluids. *Phys. Rev. Lett.* **95**, 215302.

Kivotides, D., Barenghi, C. F. & Sergeev, Y. A. 2006*a* Numerical calculation of the interaction of superfluid vortices and a rigid sphere. *J. Low Temp. Phys.* **144**, 121–134.

Kivotides, D., Barenghi, C. F. & Sergeev, Y. A. 2006*b* Physics of solid particles in thermal counterflow. *Europhys. Lett.* **73**, 733–739.

Kivotides, D., Barenghi, C. F., Mee, A. J. & Sergeev, Y. A. 2007*a* Interaction of solid particles with a tangle of vortex filaments in a viscous fluid. *Phys. Rev. Lett.* **99**, 074501.

Kivotides, D., Barenghi, C. F. & Sergeev, Y. A. 2007*b* Collision of a tracer particle and a quantized vortex in superfluid helium: self-consistent calculations. *Phys. Rev.* B **75**, 212502.

Kivotides, D., Barenghi, C. F. & Sergeev, Y. A. 2008 Interactions between particles and quantized vortices in superfluid helium. *Phys. Rev.* B **77**, 014527.

Kozik, E. & Svistunov, B. 2004 Scale-separation scheme for simulating superfluid turbulence: Kelvin-wave cascade. *Phys. Rev. Lett.* **92**, 035301.

Nazarenko, S. & West, R. J. 2003 Analytical solution for nonlinear Schroedinger vortex reconnection. *J. Low Temp. Phys.* **132**, 1.

Poole, D. R., Barenghi, C. F., Sergeev, Y. A. & Vinen, W. F. 2005 The motion of tracer particles in helium II. *Phys. Rev.* B **71**, 064514.

Schwarz, K. W. 1974 Spherical probes and quantized vortices: hydrodynamic formalism and simple applications. *Phys. Rev.* A **10**, 2306.

Schwarz, K. W. 1985 Three-dimensional vortex dynamics in superfluid ^{4}He: line–line and line–boundary interactions. *Phys. Rev.* B **31**, 5782.

Tsubota, M. & Maekawa, S. 1993 Pinning and depinning of two quantized vortices in superfluid ^{4}He. *Phys. Rev.* B **47**, 12040.

Vinen, W. F. & Niemela, J. J. 2002 Quantum turbulence. *J. Low Temp. Phys.* **129**, 213.

Vinen, W. F., Tsubota, M. & Mitani, A. 2003 Kelvin-wave cascade on a vortex in superfluid 4He at a very low temperature. *Phys. Rev. Lett.* **91**, 135301.

deWaele, A. T. A. M. & Aarts, R. G. K. M. 1994 Route to vortex reconnection. *Phys. Rev. Lett.* **72**, 482.

Winckelmans, G. S. & Leonard, A. 1993 Contributions to vortex particle methods for the computation of three-dimensional incompressible unsteady flows. *J. Comput. Phys.* **109**, 247.

Zhang, T. & VanSciver, S. W. 2005 Large-scale turbulent flow around a cylinder in counterflow superfluid 4He (He (II)). *Nature Phys.* **1**, 36–38.

Zhang, T., Celik, D. & VanSciver, S. W. 2004 Tracer particles for applications to PIV studies of liquid helium. *J. Low Temp. Phys.* **134**, 985–1000.

https://doi.org/10.1017/S0022112008001559 Published online by Cambridge University Press